9-7-2015

Experimentally Generating Any Desired Partially Coherent Schell-model Source Using Phase-only Control

Milo W. Hyde IV
Air Force Institute of Technology

Santasri Basu
Air Force Institute of Technology

David G. Voelz
Air Force Institute of Technology

Xifeng Xiao
New Mexico State University

Recommended Citation

Hyde, M. W., Basu, S., Voelz, D. G., & Xiao, X. (2015). Experimentally generating any desired partially coherent Schell-model source using phase-only control. Journal of Applied Physics, 118(9), 093102. https://doi.org/10.1063/1.4929811

Journal of Applied Physics

Experimentally generating any desired partially coherent Schell-model source using phase-only control

Cite as: J. Appl. Phys. **118**, 093102 (2015); https://doi.org/10.1063/1.4929811
Submitted: 11 July 2015 . Accepted: 18 August 2015 . Published Online: 01 September 2015

Milo W. Hyde, Santasri Basu, David G. Voelz, and Xifeng Xiao

Experimentally generating any desired partially coherent Schell-model source using phase-only control

Milo W. Hyde IV,[1,a)] Santasri Basu,[2,b)] David G. Voelz,[3,c)] and Xifeng Xiao[3,d)]
[1]*Department of Electrical and Computer Engineering, Air Force Institute of Technology Dayton, Ohio 45433, USA*
[2]*Department of Engineering Physics, Air Force Institute of Technology Dayton, Ohio 45433, USA*
[3]*Klipsch School of Electrical and Computer Engineering, New Mexico State University, Las Cruces, New Mexico 88003, USA*

(Received 11 July 2015; accepted 18 August 2015; published online 1 September 2015)

A technique is presented to produce any desired partially coherent Schell-model source using a single phase-only liquid-crystal spatial light modulator (SLM). Existing methods use SLMs in combination with amplitude filters to manipulate the phase and amplitude of an initially coherent source. The technique presented here controls both the phase and amplitude using a single SLM, thereby making the amplitude filters unnecessary. This simplifies the optical setup and significantly increases the utility and flexibility of the resulting system. The analytical development of the technique is presented and discussed. To validate the proposed approach, experimental results of three partially coherent Schell-model sources are presented and analyzed. A brief discussion of possible applications is provided in closing.
[http://dx.doi.org/10.1063/1.4929811]

I. INTRODUCTION

For the past decade, the propagation and scattering of partially coherent light has been a very active area of research. For example, numerous published articles exist predicting the polarization, coherence, and beam shape of partially coherent light after propagating through free space and random media[1–10] or scattering from deterministic and random objects/media.[11–21] Much work has also been performed exploiting coherence to control beam shape[22–30] and even as an encoding scheme for holography.[31] Excellent reviews and more in-depth discussions of these topics can be found in Refs. 32–38.

With the many possible applications of partially coherent beams (e.g., free-space optical communications, particle trapping, etc.), techniques to synthesize them have naturally followed. A vast majority of this work has focused on generating Gaussian Schell-model (GSM) sources and their many variants.[28–30,39–51] These techniques can roughly be divided into two groups—those which exploit the van Cittert-Zernike theorem[32,50–52] and most relevant to this work, those which use diffusers or spatial light modulators (SLMs) to produce GSM sources.[28–30,39–47,49]

The SLM-based synthesis techniques predominately use phase-only SLMs because of their widespread commercial availability. Using phase-only SLMs to produce Schell-model sources has two main drawbacks. The first is that another optical element is required to control the amplitude of the source, thus complicating the optical setup. For GSM synthesizers, this element is naturally a Gaussian amplitude filter.[28–30,39,40,44–47,49–51] For more general source shapes, another SLM (either amplitude or phase-only) could be used;[53–56] however, aligning the SLMs can be difficult and is a potential source of error.

The second drawback is that one is generally limited to producing sources with Gaussian-shaped coherence functions since the phase imparted to the field after transmitting through the diffuser or SLM is a Gaussian random variable.[39,49,52] References 57 and 58 show the effects on the far-zone mean irradiance when non-Gaussian coherence functions are used in combination with Gaussian phase screens. Even with this shortcoming, the variety of sources which can be produced is quite impressive;[28–30,40,44–47] however, some sources cannot be generated because of the aforementioned underlying Gaussian statistics.

Very recently, techniques to synthesize general Schell-model sources have been proposed.[26,27] These approaches employed a complex transmittance screen (termed a complex screen hereafter), where both the amplitude and phase of the initially coherent field were manipulated. In theory, since both the amplitude and phase are controlled, any desired partially coherent source can be created. In Refs. 26 and 39, the complex screen approach is presented as a computational-only method. This is because precisely controlling amplitude and phase in the laboratory is difficult, i.e., one needs amplitude filters or another SLM as previously stated. In Ref. 27, experimental results were presented; however, only the non-Gaussian phases of the complex screens were utilized to produce desired far-zone mean irradiance patterns; the coherence of the field in the far-zone was not considered.

In this paper, the experimental generation of any desired partially coherent source using a single phase-only SLM is

[a)]Electronic mail: milo.hyde@afit.edu
[b)]Electronic mail: santasri.basu.ctr.in@afit.edu
[c)]Electronic mail: davvoelz@nmsu.edu
[d)]Electronic mail: xixiao@nmsu.edu

presented. Section II presents the theory underpinning the approach: First, the requisite background of the complex screen method is presented. Second, amplitude control using a phase-only SLM is discussed, namely, the diffraction efficiency of an artificial sawtooth phase grating is manipulated to produce the desired amplitude pattern. Last, the phase-only SLM command to produce one instance of a complex screen partially coherent source is discussed.

It must be noted that phase-only amplitude-control has been presented in numerous prior publications—the papers most relevant to this work are Refs. 59–65. Here, the phase-only amplitude-control technique described in Refs. 59–63 is utilized; Refs. 64 and 65 use a different approach. Although phase-only amplitude control is not novel, the analytical development of the phase-only amplitude-control technique described in the aforementioned references is presented because it is relevant in implementing the complex screen method. References 59–63 derived the scattered field from a sawtooth grating assuming that there were an infinite number of SLM pixels per sawtooth. Here, the scattered field from a sawtooth grating formed from a finite number of SLM pixels is derived. It is shown that the true theoretical scattered-field relation converges quickly to the asymptotic expression given in Refs. 59–63. The number of SLM pixels per sawtooth required for the simpler asymptotic scattered-field relation to be accurate is discussed.

Experimental results of three partially coherent sources are presented in Section III. The first is a GSM source variant that has been theoretically analyzed in past literature.[22,36] The experimental results are compared to the theoretical predictions to validate the proposed approach. The second and third partially coherent sources are sources which cannot be synthesized using existing techniques. These results are presented to demonstrate the flexibility and applicability of the technique. Finally, this paper is concluded with a brief summary of the presented research, including contributions and applications.

II. THEORY

In this section, the theory supporting the laboratory implementation of the complex screen method for generating partially coherent sources using a single phase-only SLM is presented. The spatially partially coherent sources that are generated are Schell-model sources, where the cross-spectral density W takes the form

$$W(\boldsymbol{\rho}_1,\boldsymbol{\rho}_2,\omega) = \langle U(\boldsymbol{\rho}_1,\omega)U^*(\boldsymbol{\rho}_2,\omega)\rangle = \sqrt{S(\boldsymbol{\rho}_1,\omega)}\sqrt{S(\boldsymbol{\rho}_2,\omega)}\mu(\boldsymbol{\rho}_1-\boldsymbol{\rho}_2,\omega), \quad (1)$$

where U is the scalar optical field, S is the spectral density, μ is the spectral degree of coherence, $\boldsymbol{\rho} = \hat{\boldsymbol{x}}x + \hat{\boldsymbol{y}}y$, ω is the radian frequency, and $*$ denotes the complex conjugate.[32,33,36] Note that $S \geq 0$ and $|\mu| \leq 1$ for all $\boldsymbol{\rho}$. Hereafter, the dependence of W, U, S, and μ on ω is suppressed.

A. Complex screen method

In the complex screen method for generating Schell-model sources, a random screen with the proper spatial statistics is applied to a coherent source field. A single instance of a complex screen field takes the form

$$U(\boldsymbol{\rho}) = \sqrt{S(\boldsymbol{\rho})}T(\boldsymbol{\rho}), \quad (2)$$

where T is the complex screen (both amplitude and phase are affected) and is a sample function drawn from a zero-mean, complex, Gaussian random process.[27,39]

Taking the autocorrelation of Eq. (2) yields

$$\langle U(\boldsymbol{\rho}_1)U^*(\boldsymbol{\rho}_2)\rangle = \sqrt{S(\boldsymbol{\rho}_1)}\sqrt{S(\boldsymbol{\rho}_2)}\langle T(\boldsymbol{\rho}_1)T^*(\boldsymbol{\rho}_2)\rangle. \quad (3)$$

By comparing this expression with Eq. (1), one deduces that

$$\langle T(\boldsymbol{\rho}_1)T^*(\boldsymbol{\rho}_2)\rangle = \mu(\boldsymbol{\rho}_1-\boldsymbol{\rho}_2). \quad (4)$$

Although the preceding analysis is simple, the implication is quite important. It states that *any* Schell-model source can be generated if $\langle|U|^2\rangle = S$, and if T can be synthesized with an autocorrelation equal to the spectral degree of coherence μ.

It must be reiterated that generating any Schell-model source is feasible only when the amplitude and phase are manipulated via T. Consider the traditional phase screen approach, easily implemented on an SLM, where $T = \exp(\mathrm{j}\phi)$ and ϕ is a sample function drawn from a zero-mean, real, Gaussian random process ($\mathrm{j} = \sqrt{-1}$). Equation (4) then becomes

$$\begin{aligned}\langle U(\boldsymbol{\rho}_1)U^*(\boldsymbol{\rho}_2)\rangle &= \sqrt{S(\boldsymbol{\rho}_1)}\sqrt{S(\boldsymbol{\rho}_2)}\langle e^{\mathrm{j}\phi(\boldsymbol{\rho}_1)}e^{-\mathrm{j}\phi(\boldsymbol{\rho}_2)}\rangle \\ &= \sqrt{S(\boldsymbol{\rho}_1)}\sqrt{S(\boldsymbol{\rho}_2)}\exp\{-\sigma_\phi^2[1-\gamma(\boldsymbol{\rho}_1-\boldsymbol{\rho}_2)]\},\end{aligned} \quad (5)$$

where σ_ϕ^2 is the variance of ϕ and γ is the normalized autocorrelation function of ϕ.[39,52]

By comparing Eq. (5) to Eq. (1), one can clearly see that the traditional phase screen method is not as powerful as the complex screen approach when it comes to generating Schell-model sources. Practically, the only thing that can be done with the coherence function in Eq. (5) is to assume that γ is Gaussian and $\sigma_\phi^2 \gg 1$. As a consequence of this latter assumption, the $1-\gamma$ term in the exponential must be small for the coherence function to possess a significant value. This prompts expanding γ in a Maclaurin series and retaining only the first two terms. Subsequent simplification of the resulting expression yields a Gaussian coherence function.[39,57,58]

It might be possible with traditional phase screens to match the flexibility of the complex screen approach, if ϕ is drawn from a non-Gaussian random process; however, a Gaussian random process is one of the few (if only) random processes where the required moments, in particular, the moment in Eq. (5), can be computed in closed form. A non-Gaussian phase screen technique similar to that used in Ref. 27 could be employed here; however, as was shown in that paper, the desired spectral degree of coherence μ and the achievable μ are not equal (they are approximately equal). Before progressing to how the random amplitude of U is reproduced using a single phase-only SLM, a brief summary of how T are synthesized is presented.

B. *T* synthesis

Let T and $\tilde{T}$ be Fourier transform pairs, i.e.,

$$\begin{aligned}\tilde{T}(\boldsymbol{f}) &= \int_{-\infty}^{\infty}\int T(\boldsymbol{\rho})e^{-\mathrm{j}2\pi\boldsymbol{f}\cdot\boldsymbol{\rho}}\mathrm{d}^2\rho \\ T(\boldsymbol{\rho}) &= \int_{-\infty}^{\infty}\int \tilde{T}(\boldsymbol{f})e^{\mathrm{j}2\pi\boldsymbol{f}\cdot\boldsymbol{\rho}}\mathrm{d}^2 f,\end{aligned} \tag{6}$$

where $\boldsymbol{f} = \hat{\boldsymbol{x}}f_x + \hat{\boldsymbol{y}}f_y$ is the spatial frequency vector. Recall that T is a sample function drawn from a zero-mean, complex, Gaussian random process such that

$$\begin{aligned}\langle T(\boldsymbol{\rho})\rangle &= 0 \\ \langle T(\boldsymbol{\rho}_1)T^*(\boldsymbol{\rho}_2)\rangle &= \mu(\boldsymbol{\rho}_1 - \boldsymbol{\rho}_2).\end{aligned} \tag{7}$$

Note that T is a homogeneous random field; therefore, by the spatial equivalent of the Wiener-Khinchin theorem

$$\langle T(\boldsymbol{\rho}_1)T^*(\boldsymbol{\rho}_2)\rangle = \int_{-\infty}^{\infty}\int \Phi^T(f)e^{\mathrm{j}2\pi\boldsymbol{f}\cdot(\boldsymbol{\rho}_1-\boldsymbol{\rho}_2)}\mathrm{d}^2 f, \tag{8}$$

where Φ^T is the power spectral density of T.[52]

Expanding T in a Fourier series yields

$$T(\boldsymbol{\rho}) = \sum_{m,n}\mathcal{T}[m,n]e^{\mathrm{j}\frac{2\pi}{L}mx}e^{\mathrm{j}\frac{2\pi}{L}ny}, \tag{9}$$

where $\mathcal{T}$ are zero-mean, circular complex Gaussian Fourier series coefficients, m, n are the discrete spatial frequency indices of the matrix $\mathcal{T}$, and L is the physical size of the discrete grid. Taking the autocorrelation of Eq. (9) and comparing that result to Eq. (8) implies that

$$\langle|\mathcal{T}[m,n]|^2\rangle = \Phi^T\left[\frac{m}{L},\frac{n}{L}\right]\frac{1}{L^2}. \tag{10}$$

Note that $\langle|\mathcal{T}|^2\rangle$ is equivalent to the variance of the Fourier series coefficients. Since $\mathcal{T}$ are circular complex Gaussian, the variances of the real and imaginary parts of $\mathcal{T}$ are equal,[52] thus,

$$\sigma^2_{\mathrm{Re}(\mathcal{T})} = \sigma^2_{\mathrm{Im}(\mathcal{T})} = \Phi^T\left[\frac{m}{L},\frac{n}{L}\right]\frac{1}{2L^2}. \tag{11}$$

Combining these results, a complex screen T can be generated by

$$T[i,j] = \sum_{m,n} r[m,n]\sqrt{\Phi^T\left[\frac{m}{L},\frac{n}{L}\right]\frac{1}{2L^2}}e^{\mathrm{j}\frac{2\pi}{N}mi}e^{\mathrm{j}\frac{2\pi}{N}nj}, \tag{12}$$

where i, j are the discrete spatial indices of the screen T, N is the number of points per side of the screen, and r is a $N\times N$ matrix of zero-mean, unit-variance, circular complex Gaussian random numbers.[39]

Equation (12) is in the form of a discrete inverse Fourier transform; and therefore, for computational efficiency, the fast Fourier transform algorithm is commonly used to synthesize T.

C. Controlling amplitude

In this section, the phase-only amplitude-control technique utilized in this research is theoretically developed. The general concept is to use the SLM to create a periodic phase grating that produces the desired field in the first diffraction order. By manipulating the characteristics of the grating, both the amplitude and phase of the field can be controlled.

The analysis begins with the derivation of the far-zone scattered electric field $\boldsymbol{E}^s$ from a discrete periodic sawtooth grating. This result is used to derive the ratio $\boldsymbol{E}^s(h)/\boldsymbol{E}^s(h=\lambda)$, which provides the relationship between the sawtooth height h and the field (both amplitude and phase) in the first diffraction order.

1. Far-zone scattered field from sawtooth grating

Consider the scattering geometry depicted in Fig. 1. The figure shows a z-polarized (vertically polarized) incident field scattered from a discrete periodic sawtooth grating. Each sawtooth is $L\times h$ and composed of $N+1$ rectangular pulses (physically SLM pixels) of width d. There are a total of $M+1$ sawteeth in the grating. The scattered field is observed in the far zone and in the specular direction with respect to the sawteeth when $h=\lambda$ (i.e., in the direction of the first diffraction order). Note that the incident-field polarization state and observation direction match the experimental setup discussed in Section III. To simplify the analysis, the grating is assumed to be perfecting reflecting (i.e., a

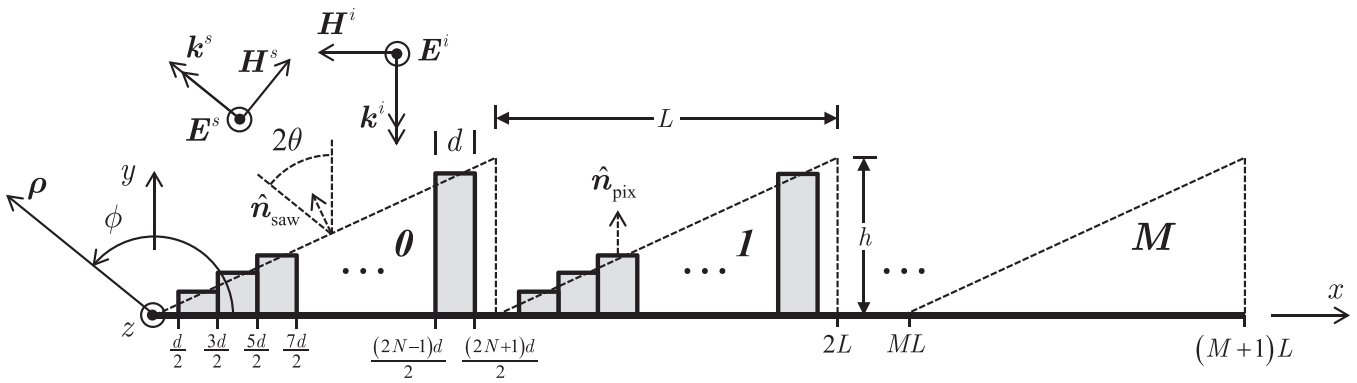

FIG. 1. Sawtooth phase grating scattering geometry.

perfect electric conductor) and invariant in the z direction. These simplifications do not affect the result.

The incident field is assumed to be a plane wave, where the incident electric $\boldsymbol{E}^i$ and magnetic $\boldsymbol{H}^i$ fields take the form

$$\begin{aligned}\boldsymbol{E}^i &= \hat{\boldsymbol{z}}E_0 e^{\mathrm{j}ky}\\ \boldsymbol{H}^i &= -\hat{\boldsymbol{x}}\frac{E_0}{\eta}e^{\mathrm{j}ky}.\end{aligned} \tag{13}$$

Here, E_0 is the amplitude of the incident electric field, η is the intrinsic impedance of vacuum (approximately 377 Ω), and $k = 2\pi/\lambda$ is the wavenumber. Note that the $\exp(\mathrm{j}\omega t)$ convention is utilized and subsequently suppressed.

The far-zone scattered electric field $\boldsymbol{E}^s$ is found using the far-zone vector potential $\boldsymbol{N}$[66]

$$\boldsymbol{E}^s \approx -\sqrt{\frac{\mathrm{j}k}{8\pi}}\frac{e^{-\mathrm{j}k\rho}}{\sqrt{\rho}}\frac{1}{\eta_0}\left(\hat{\phi}\hat{\phi}+\hat{z}\hat{z}\right)\cdot\boldsymbol{N}. \tag{14}$$

The potential $\boldsymbol{N}$ is found using the superposition principle, i.e.,

$$\begin{aligned}\boldsymbol{N} &= \sum_{m=0}^{M}\sum_{n=0}^{N}\boldsymbol{N}_{m,n}\\ \boldsymbol{N}_{m,n} &= \int_{C_{m,n}}\boldsymbol{J}_{m,n}(\boldsymbol{\rho}')e^{-jk\hat{\boldsymbol{\rho}}\cdot\boldsymbol{\rho}'_n}\mathrm{d}C',\end{aligned} \tag{15}$$

where m is the sawtooth index, n is the pixel index, $C_{m,n}$ denotes the contour along the nth pixel in the mth sawtooth, and $\boldsymbol{J}_{m,n}$ is the electric current induced on the nth pixel in the mth sawtooth by the total field $\boldsymbol{E} = \boldsymbol{E}^i + \boldsymbol{E}^s$.[66] Since $d/\lambda \approx 23$ (details provided in Section III), the physical optics (POs) approximation[67] is used to find $\boldsymbol{J}_{m,n}$

$$\begin{aligned}\boldsymbol{J}_{m,n} &\approx 2\hat{\boldsymbol{n}}_{\mathrm{pix}}\times\boldsymbol{H}^i|_{\boldsymbol{\rho}=\boldsymbol{\rho}'_n}\\ &= \hat{\boldsymbol{z}}\frac{2E_0}{\eta}\exp\left(\mathrm{j}kn\frac{h}{L}d\right),\end{aligned} \tag{16}$$

where $\hat{\boldsymbol{n}}_{\mathrm{pix}} = \hat{\boldsymbol{y}}$ is the unit-normal vector with respect to the SLM pixels (see Fig. 1).

Substituting Eq. (16) into Eq. (15), evaluating the simple, yet tedious integrals, and simplifying yields

$$\begin{aligned}\boldsymbol{N} = \hat{\boldsymbol{z}}\frac{2E_0}{\eta}d\,\mathrm{sinc}\left(k\frac{d}{2}\hat{\boldsymbol{\rho}}\cdot\hat{\boldsymbol{x}}\right)\left[\sum_{m=0}^{M}\exp(\mathrm{j}kmL\hat{\boldsymbol{\rho}}\cdot\hat{\boldsymbol{x}})\right]\\ \times\left[\sum_{n=0}^{N}\exp(\mathrm{j}knd\psi)\right],\end{aligned} \tag{17}$$

where $\psi = \hat{\boldsymbol{\rho}}\cdot\hat{\boldsymbol{x}} + (h/L)(1+\hat{\boldsymbol{\rho}}\cdot\hat{\boldsymbol{y}})$.

As expected from antenna array theory, Eq. (17) is the product of the far-zone field pattern from a single array element and the array factor.[68] In this case, the $\mathrm{sinc}(x) = \sin(x)/x$ term is the element pattern, i.e., the far-zone field scattered from a rectangular pulse of width d. The product of the summations comprises the array factor, where the m and n summations are the sawtooth and SLM pixel contributions, respectively.

Using trigonometric identities, the m and n summations can be expressed in a more compact form[68]

$$\begin{aligned}\boldsymbol{N} = \hat{\boldsymbol{z}}\frac{2E_0}{\eta}d\,\mathrm{sinc}\left(k\hat{\boldsymbol{\rho}}\cdot\hat{\boldsymbol{x}}\frac{d}{2}\right)\exp\left[\mathrm{j}\frac{k}{2}(\hat{\boldsymbol{\rho}}\cdot\hat{\boldsymbol{x}}ML+\psi Nd)\right]\\ \times\frac{\sin\left[\frac{kL}{2}\hat{\boldsymbol{\rho}}\cdot\hat{\boldsymbol{x}}(M+1)\right]}{\sin\left(\frac{kL}{2}\hat{\boldsymbol{\rho}}\cdot\hat{\boldsymbol{x}}\right)}\frac{\sin\left[\frac{kd}{2}\psi(N+1)\right]}{\sin\left(\frac{kd}{2}\psi\right)}.\end{aligned} \tag{18}$$

The far-zone scattered electric field $\boldsymbol{E}^s$ can be found by substituting Eq. (18) into Eq. (14). Since $\boldsymbol{E}^s \propto \boldsymbol{N}$ and a ratio of scattered fields is ultimately desired, this step is superfluous and not performed here.

2. Ratio of scattered fields

Using Eq. (18), the ratio $\boldsymbol{E}^s(h)/\boldsymbol{E}^s(h=\lambda) = E_z^s(h)/E_z^s(h=\lambda)$, which gives the relationship between h and the field in the first diffraction order, can be derived.

Relating the angle of incidence and reflection θ to the observation angle ϕ via simple geometry yields the following relations:

$$\begin{aligned}\hat{\boldsymbol{\rho}}\cdot\hat{\boldsymbol{x}} &= \cos\phi = -2\frac{\lambda}{L}\frac{1}{1+(\lambda/L)^2}\\ \psi &= \hat{\boldsymbol{\rho}}\cdot\hat{\boldsymbol{x}} + \frac{h}{L}(1+\hat{\boldsymbol{\rho}}\cdot\hat{\boldsymbol{y}}) = \cos\phi + \frac{h}{L}(1+\sin\phi)\\ &= \frac{2}{L}\frac{h-\lambda}{1+(\lambda/L)^2}.\end{aligned} \tag{19}$$

Substituting these into Eq. (18) and computing $E_z^s(h)/E_z^s(h=\lambda)$ produces the desired result, i.e.,

$$\begin{aligned}\frac{E_z^s(h)}{E_z^s(h=\lambda)} = \frac{1}{N+1}\frac{\sin\left(2\pi\frac{1-h/\lambda}{1+(\lambda/L)^2}\right)}{\sin\left(\frac{2\pi}{N+1}\frac{1-h/\lambda}{1+(\lambda/L)^2}\right)}\\ \times\exp\left[-\mathrm{j}2\pi\frac{N}{N+1}\frac{1-h/\lambda}{1+(\lambda/L)^2}\right].\end{aligned} \tag{20}$$

This is the true relation, within the accuracy of the PO approximation, for the field in the first diffraction order versus sawtooth height h.

Before progressing to the SLM command, a few more aspects of this result warrant discussion. Since $d \gg \lambda$, it stands to reason that $L \gg \lambda$; therefore, $1+(\lambda/L)^2 \approx 1$. The factor of 2 in the sine and exponential arguments is a result of modeling the SLM as a reflection grating. It is due to the two-way path light traverses as it reflects from the grating. SLMs are calibrated to determine how SLM command maps to applied phase φ. In the process of making these calibration measurements, the factor of 2 in Eq. (20) is incorporated into the measured φ. Thus, the factor of 2 must be removed from Eq. (20) so that the correct phase is applied by the SLM. Finally, if the number of pixels per sawtooth becomes large, Eq. (20) becomes

$$\lim_{N\to\infty}\frac{E_z^s(h)}{E_z^s(h=\lambda)} = H(h)\exp\left[-\mathrm{j}P(h)\right] = \mathrm{sinc}[\pi(1-h/\lambda)]\exp[-\mathrm{j}\pi(1-h/\lambda)]. \quad (21)$$

This is the field relation given in Refs. 59–63 and is correct for a continuous sawtooth grating. Equation (20) rapidly converges to Eq. (21), such that for $N>4$, $H(h)$ can be inverted to determine the required h. Equations (20) and (21) were experimentally verified using an eight pixel per sawtooth grating. The sinc-like amplitude behavior versus h held for irradiances captured in both the far-zone and source-plane cameras (SPCs) (described in detail in Section III). These experimental results are not presented here for the sake of brevity. Note that the grating imparts an unwanted phase P to the field. As shown below, it can be removed with a corresponding SLM command.

D. SLM command

With the proceeding analysis, one can determine the SLM command to generate a single instance of a general Schell-model source. The first step is to generate a complex screen field instance U [recall Eq. (2)], which requires a desired spectral density S and a complex screen T synthesized in the manner outlined in Section II B. The required sawtooth heights h are found by solving $h = H^{-1}(|U|)$. The SLM command C is

$$C[i,j] = D[\arg(\exp\{\mathrm{j}[G(h)+\arg(T)+F(h)]\})], \quad (22)$$

where D is the function that maps phases to digital commands, G is the function that forms the two-dimensional sawtooth phase grating with the appropriate heights h, and F is the function that creates two-dimensional P. The purpose of F is to remove the unwanted phase imparted to the field by G. The desired U is the first diffraction order.

The sawteeth making up the grating will have the same length L, but, in general, have different heights. The grating can be formed in the x direction (as shown in Fig. 1), the y direction, or in both directions. The grating period $L=(N+1)d$ determines the fidelity of the sawtooth grating (a larger L better approximates a continuous sawtooth) as well as the relative separation of the diffraction orders (a smaller L provides wider diffraction order separation). Therefore, L must be chosen such that a high-fidelity $|U|$ can be produced, while providing enough separation between the orders so that the desired first order can be effectively separated from the others (typically using a spatial filter) with little corruption. Ultimately, the choice of L (really N) will depend heavily on U and the experimental setup.

III. EXPERIMENTAL RESULTS

A. Experimental setup

Figure 2 shows a schematic of the experimental setup. Light leaves a 2 mW 632.8 nm HeNe laser and is expanded 20 times before passing through a half-wave plate (HWP) and a linear polarizer (LP). The linear polarizer and half-wave plate serve to align the laser's linear polarization state

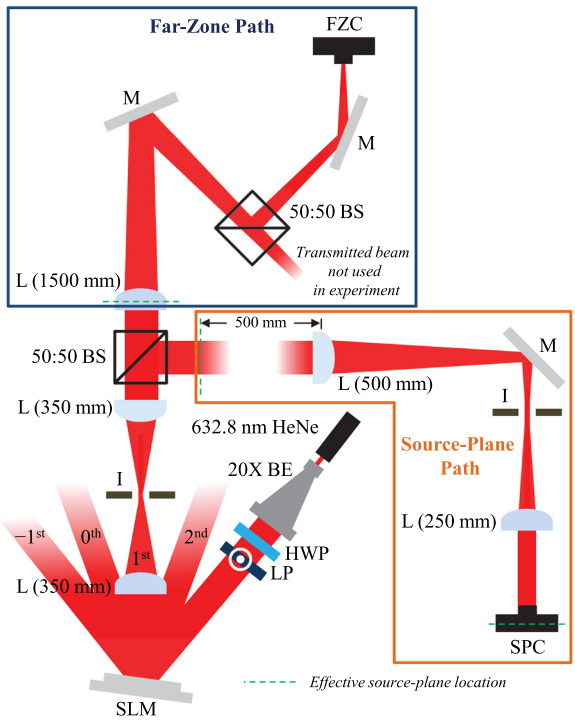

FIG. 2. Schematic of the experimental setup—BE is the beam expander, HWP is the half-wave plate, LP is the linear polarizer, SLM is the spatial light modulator, L is the lens, I is the iris, BS is the beam splitter, M is the mirror, FZC is the far-zone camera, and SPC is the source-plane camera.

to the command polarization state of the SLM (accomplished using the linear polarizer set in the vertical direction) and to control the power incident on the SLM (accomplished using the half-wave plate in combination with the linear polarizer).

After traversing the half-wave plate and linear polarizer, the light is incident on the SLM. The SLM used here is a 512×512 Boulder Nonlinear Systems (BNS) model P512-0635 with a 15 μm pitch.[69] As shown, light scatters from the SLM into multiple diffraction orders. Here, the light in the first order is used and ultimately directed to the sensors. The other orders are either physically blocked with the irises or miss the detectors.

Here, eight SLM pixels per sawtooth were used. This choice provided the necessary amplitude fidelity, while sufficiently separating the diffraction orders such that the desired first order could be passed through the optical system with little degradation from the other orders. The SLM grating was applied in both the x and y directions. The BNS SLM utilized in the experiments has a fill factor of 83.4%.[69] The "dead-space" between pixels results in a very bright, uncontrollable zeroth diffraction order which forms a sinc-like pattern in the far zone. Applying the grating in both the x and y directions moves the desired first order away from the zeroth-order sinc side lobes (oriented along the x and y directions), thus minimizing corruption.

After scattering from the SLM, the light enters a 4-f system composed of two 350 mm lenses. At the focus of the first 350 mm lens, an iris (I) is used to block all orders except the desired first order. After passing through the second 350 mm lens, the light is split by a 50:50 beam splitter (BS) and directed along two paths.

The first path, called the far-zone path, consists of a 1500 mm lens, which is placed at the focus of the second 350 mm lens, and a camera. The far-zone camera (FZC) is placed at the focus of the 1500 mm lens. Note that the 4-*f*/iris system effectively places the source plane (or the desired U) at the 1500 mm lens location (see corresponding green dashed line in Fig. 2); therefore, the far-zone camera captures the far-zone irradiance pattern of U. The far-zone camera is a Lumenera LU125M camera—1280 × 1024 with a 6.7 μm pitch.[70]

The second path, the source-plane path, consists of a 500 mm–250 mm lens system (the lenses are separated by 750 mm) and a camera. The 500 mm lens is placed 500 mm from the focus of the second 350 mm lens. Another iris is used at the focus of the 500 mm lens to pass only the desired first diffraction order. The SPC is placed at the focus of the 250 mm lens. Again note that the 4-*f*/iris system effectively places the source plane (or the desired U) 500 mm in front of the 500 mm lens (see corresponding green dashed line in Fig. 2). The 500 mm–250 mm lens/iris system places demagnified (by a factor of two) U at the location of the source-plane camera (see corresponding green dashed line in Fig. 2); therefore, the source-plane camera captures the irradiance of U at 1/2 size. Like the far-zone camera, the source-plane camera is a Lumenera LU125M camera.

By collecting both the source-plane and far-zone irradiance patterns, the accuracy of the complex screen approach for generating partially coherent Schell-model sources can be determined. It is quite clear from Eqs. (3) and (4) that the spectral density S can be determined from averaging source-plane irradiances. Therefore, the summed source-plane camera images show how accurately the spectral density S of the desired Schell-model source is produced. Simple analysis shows that the far-zone spectral density is predominately driven by the spectral degree of coherence μ.[32,33,36] Therefore, the summed far-zone camera images show how accurately the spectral degree of coherence μ of the desired Schell-model source is produced. In the experimental results to follow, 5000 source-plane camera and far-zone camera images were used to compute the source-plane and far-zone spectral densities.

In addition to the experimental results, simulation results are also presented below. For the simulations, the equipment and setup described above performed perfectly, i.e., no noise, aberrations, jitter, etc. These results are presented to demonstrate the best that can be achieved using the apparatus depicted in Fig. 2. Like in the experiments, 5000 simulated source-plane camera and far-zone camera images were used to compute the source-plane and far-zone spectral densities.

B. Schell-model source results

1. Bessel-Gaussian-correlated Schell-model (BGSM) source

The first Schell-model source experimentally produced was a BGSM source

$$W(\boldsymbol{\rho}_1,\boldsymbol{\rho}_2)=\exp\left(-\frac{\rho_1^2+\rho_2^2}{4\sigma^2}\right)\times J_0\left(\frac{\beta}{\delta}|\boldsymbol{\rho}_1-\boldsymbol{\rho}_2|\right)\exp\left(-\frac{|\boldsymbol{\rho}_1-\boldsymbol{\rho}_2|^2}{2\delta^2}\right), \quad (23)$$

where σ and δ are the root-mean-square widths of the spectral density and the Gaussian component of the spectral degree of coherence, respectively, β is the real constant, and J_0 is the zeroth-order Bessel function of the first kind.[22,36] It is clear from the above expression that the source-plane spectral density $S=W(\boldsymbol{\rho},\boldsymbol{\rho})$ is Gaussian.

With the BGSM cross-spectral density W provided above, a closed-form expression for the far-zone W can easily be derived.[22,36] In the experiments, the far-zone BGSM W is produced by using a lens, where the lens and source plane are collocated. This scenario is equivalent to the classic Fourier optics problem of an input placed against a lens.[71] Omitting the details for the sake of brevity, the BGSM W recorded at the focal plane of the lens is

$$W(\boldsymbol{\rho}_1,\boldsymbol{\rho}_2)=\frac{k^2\sigma^2}{2\gamma f^2}\exp\left(-\frac{\beta^2}{4\gamma\delta^2}\right)\exp\left[\frac{\mathrm{j}k}{2f}\left(\rho_1^2-\rho_2^2\right)\right]\times\exp\left[-\frac{1}{16\gamma}\left|\frac{k}{f}(\boldsymbol{\rho}_1+\boldsymbol{\rho}_2)\right|^2\right]I_0\left[\frac{\beta}{4\gamma\delta}\left|\frac{k}{f}(\boldsymbol{\rho}_1+\boldsymbol{\rho}_2)\right|\right]\times\exp\left[-\frac{1}{2}\left|\frac{k\sigma}{f}(\boldsymbol{\rho}_1-\boldsymbol{\rho}_2)\right|^2\right] \quad (24)$$

where $\gamma=1/(8\sigma^2)+1/(2\delta^2)$, f is the focal length of the lens, and I_0 is the zeroth-order modified Bessel function of the first kind. The far-zone BGSM spectral density S, which is used to validate the experimental results, is

$$S(\rho)=\frac{k^2\sigma^2}{2\gamma f^2}\exp\left(-\frac{\beta^2}{4\gamma\delta^2}\right)\exp\left(-\frac{k^2}{4\gamma f^2}\rho^2\right)I_0\left(\frac{\beta k}{2\gamma\delta f}\rho\right) \quad (25)$$

and has a distinctive ring shape.

Figure 3 shows the experimental BGSM results. The σ, δ, and β of the BGSM source were 0.4525 mm, 1.3576 mm, and 10, respectively. The rows of Fig. 3 are theoretical S [Figs. 3(a) and 3(b)]; simulated S [Figs. 3(c) and 3(d)]; instances of experimental $|U|^2$, i.e., example source-plane camera and far-zone camera images [Figs. 3(e) and 3(f)], respectively; experimental S [Figs. 3(g) and 3(h)]; and $y=0$ slices of theoretical, simulated, and experimental normalized S [Figs. 3(i) and 3(j)], respectively. The columns of the figure are source-plane S (left column) and far-zone S (right column), respectively.

The experimental S presented in Fig. 3 was formed by subtracting an estimate of the source-plane camera and far-zone camera noise floors from the raw S (negative source-plane and far-zone S values were set to zero). The noise floor estimates were obtained by averaging the values of all raw S pixels that fell below an empirically determined threshold value. Here, that threshold value was 1/5 the maximum pixel value in the raw S.

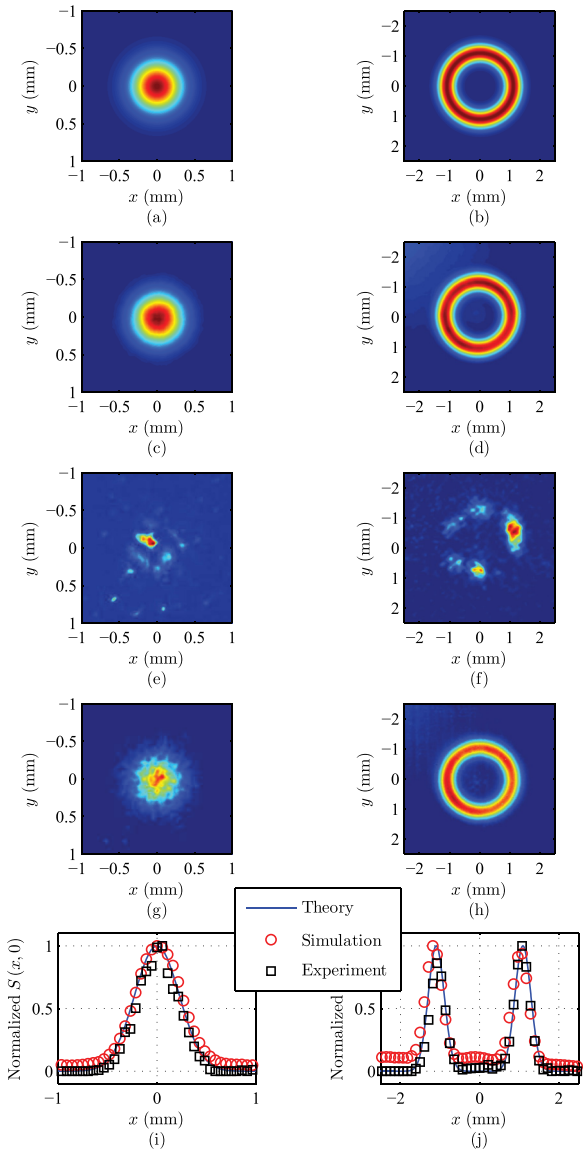

FIG. 3. BGSM results—(a) theoretical source-plane spectral density S, (b) theoretical far-zone spectral density S, (c) simulated source-plane spectral density S, (d) simulated far-zone spectral density S, (e) example source-plane camera image, (f) example far-zone camera image, (g) experimental source-plane spectral density S, (h) experimental far-zone spectral density S, (i) $y = 0$ slice of theoretical, simulated, and experimental normalized source-plane S, and (j) $y = 0$ slice of theoretical, simulated, and experimental normalized far-zone S.

Overall, the results are quite good. The agreement between the theoretical, simulated, and experimental far-zone S is excellent [Figs. 3(b), 3(d), 3(h), and 3(j)], i.e., the distinctive far-zone ring is clearly reproduced. For the source-plane S results, the theoretical and simulated results are in very good agreement [Figs. 3(a), 3(c), and 3(i)]. The agreement between the experimental source-plane S and the corresponding theoretical and simulated results is not as impressive as in the far-zone S results; however, one can clearly see the Gaussian shape in the experimental S [Figs. 3(g) and 3(i)].

The single instance source-plane and far-zone $|U|^2$ results [Figs. 3(e) and 3(f), respectively] are included to give the reader insight into the nature of the patterns that are averaged to produce the source-plane and far-zone S [Figs. 3(g) and 3(h)], respectively. They are fully developed speckle patterns.[72]

As a consequence of the complex Gaussian moment theorem,[72] the speckle sizes in the source plane and far zone are related to the radii of the source-plane and far-zone coherence functions, respectively. The BGSM source-plane and far-zone coherence functions are obtained from Eqs. (23) and (24), respectively, and are

$$\mu^{\mathrm{SP}}(|\boldsymbol{\rho}_1 - \boldsymbol{\rho}_2|) = J_0\left(\frac{\beta}{\delta}|\boldsymbol{\rho}_1 - \boldsymbol{\rho}_2|\right)\exp\left(-\frac{|\boldsymbol{\rho}_1 - \boldsymbol{\rho}_2|^2}{2\delta^2}\right)$$
$$\mu^{\mathrm{FZ}}(|\boldsymbol{\rho}_1 - \boldsymbol{\rho}_2|) = \exp\left[-\frac{1}{2}\left|\frac{k\sigma}{f}(\boldsymbol{\rho}_1 - \boldsymbol{\rho}_2)\right|^2\right]. \quad (26)$$

Assuming that the first zero of the Bessel function and the $1/e$ point are representative of the widths of μ^{SP} and μ^{FZ}, respectively, using the values of k, f, σ, β, and δ provided above, and taking into account that the source-plane camera images the source plane at 1/2 size, the theoretical source-plane and far-zone speckle sizes are approximately 0.160 mm and 0.470 mm. Note that these values are consistent with the source-plane and far-zone speckles evident in Figs. 3(e) and 3(f), respectively.

2. New Mexico State University (NMSU) Air Force Institute of Technology (AFIT) and retina fingerprint Schell-model sources

To demonstrate the flexibility of the experimental complex screen technique presented here, two Schell-model sources that could not be synthesized using existing approaches were generated. The first had source-plane and far-zone S in the shapes of the NMSU and AFIT logos, respectively. The second source had a source-plane and far-zone S that were a retina scan and fingerprint, respectively.

Figures 4 and 5 show the NMSU AFIT and retina fingerprint Schell-model source results, respectively. The layout of both figures is the same: Figs. 4(a), 4(b), 5(a), and 5(b) show the original logos/images, Figs. 4(c), 4(d), 5(c), and 5(d) show the simulated source-plane and far-zone S, respectively, and Figs. 4(e), 4(f), 5(e), and 5(f) show the experimental source-plane and far-zone S, respectively. Like in the BGSM results, the estimated noise floors (obtained in the same manner as described above) were subtracted from the raw S to form the experimental images shown in Figs. 4 and 5.

For the NMSU AFIT Schell-model source results [Fig. 4], both logos are clearly reproduced. The agreement between the simulated [Figs. 4(c) and 4(d)] and experimental results [Figs. 4(e) and 4(f)] is excellent. Recall that the simulated results represent the best that can be achieved using the experimental setup described above. Note that if one were to position the far-zone camera close to the 1500 mm lens and capture images as the camera moved back to its depicted position at the focus of the 1500 mm lens (see Fig. 2), on average, one would observe a NMSU-logo beam transform into an AFIT-logo beam.

For the retina fingerprint source results [Fig. 5], the far-zone S, i.e., the fingerprint, is successfully reproduced with a majority of the ridges clearly visible [Figs. 5(b), 5(d), and 5(f)].

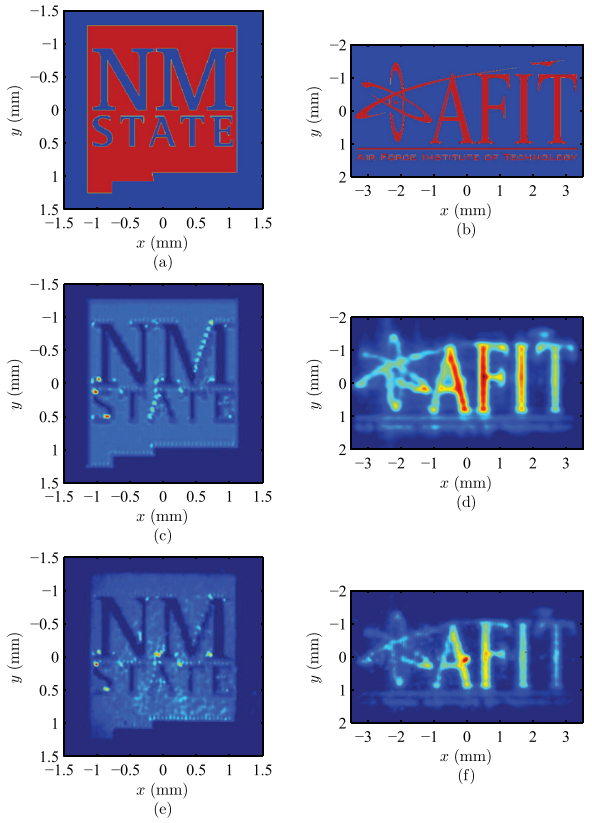

FIG. 4. NMSU AFIT Schell-model source results—(a) original NMSU logo, (b) original AFIT logo, (c) simulated source-plane spectral density S, (d) simulated far-zone spectral density S, (e) experimental source-plane spectral density S, and (f) experimental far-zone spectral density S.

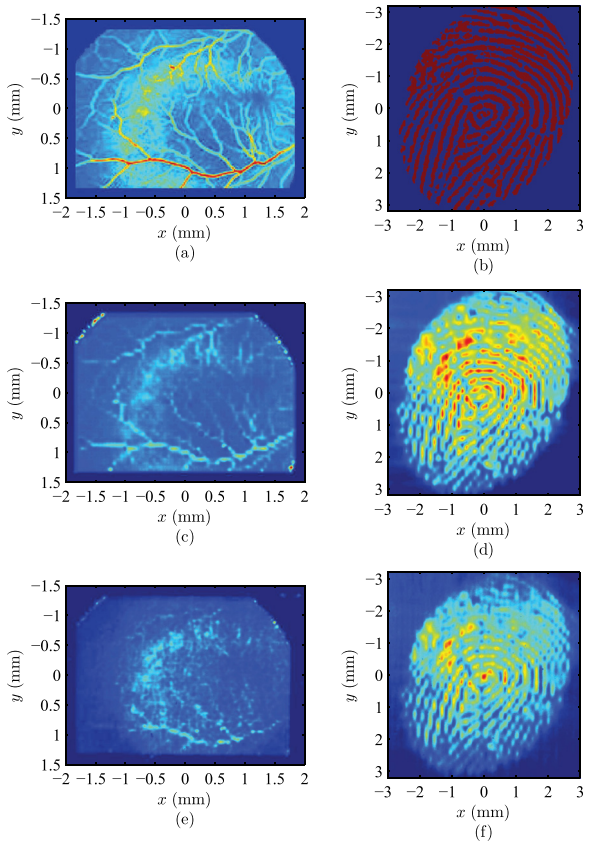

FIG. 5. Retina fingerprint Schell-model source results—(a) original retina scan image, (b) original fingerprint image, (c) simulated source-plane spectral density S, (d) simulated far-zone spectral density S, (e) experimental source-plane spectral density S, and (f) experimental far-zone spectral density S.

In contrast, many features are lost in the generated retina scan images [Figs. 5(a), 5(c), and 5(e)]. The only original image attributes that are reproduced are the large blood vessel and C-shaped bright feature at the bottom and center of the original image, respectively. The quality of the experimental source-plane S is expected since the identifying features in the retina scan image, i.e., the blood vessels, are small and similar in brightness to the image background.

The retina fingerprint source is at the limit of what can practically be produced using the equipment and apparatus depicted in Fig. 2. This statement is supported by the good agreement between the simulated and experimental results [Figs. 5(c)–5(f)]. It bears repeating that the simulated results represent the best that can be achieved using the experimental setup described above. Overall, the small drop in image quality between the simulated and experimental results is easily accounted for by experimental errors, such as optical aberrations, jitter, noise, and nonuniform SLM illumination. Note that better results are, of course, achievable with a different apparatus. Section III B 3 discusses important factors that must be considered when designing a system for a specific application.

3. Discussion

While in theory, there is no limit (with the exception of diffraction) to the quality of the Schell-model source that can be produced using the complex screen method, the size and pixel pitch of the SLM limit what can practically be achieved. As previously discussed, the source-plane speckle size is related to the radius of the source-plane coherence function. The source-plane speckles are the fundamental building blocks of the source-plane spectral density S (recall that S is formed by averaging speckle images). Thus, a high-quality source-plane S depends on the ability of the SLM to produce high-quality source-plane speckle patterns. Since the SLM forms the speckle patterns by controlling the heights of the sawteeth in the grating, it stands to reason that at least two sawteeth per speckle (spatial Nyquist criterion) are required to produce an acceptable source-plane speckle pattern. This can be difficult to achieve. For instance, the SLM used here (utilizing an eight pixel per sawtooth grating) barely satisfied this criterion (between two and three sawteeth per speckle) for the simulated and experimental source-plane S presented above. This, in addition to other common experimental errors, such as noise, aberrations, jitter, and nonuniform illumination, explains the quality of the experimental source-plane spectral density S results.

In the far zone, the quality of S is driven predominately by the ability of the SLM to produce the desired phase in the source plane.[27] To produce high-quality phase screens, 10 SLM pixels per source-plane coherence width are generally required. This criterion is relatively easy to meet in practice. For example, the SLM used here possessed at least 20 pixels

per coherence width for the simulated and experimental far-zone S generated and presented above. This explains why, in general, the far-zone S results are of a higher quality than the source-plane S results.

In a real-world application, the general system design criteria discussed in the preceding paragraphs need to be considered. Here, the goal was to present the complex screen technique and demonstrate proof of concept with no specific application in mind. The experimental results presented in Sections III B 1 and III B 2 achieve this goal.

IV. CONCLUSION

In this paper, the experimental generation of any desired partially coherent Schell-model source using a single phase-only SLM (phase-only control) was presented. This was accomplished in the laboratory by implementing the complex screen technique,[26,27] where both the amplitude and phase of an initially coherent source/field were controlled. Traditional approaches for generating Schell-model sources used SLMs in combination with amplitude filters to control both the phase and amplitude, respectively.[28–30,39,40,44–47,49–51] Here, by using a single SLM to manipulate both amplitude and phase, these filters can be removed, thereby simplifying the optical setup while significantly increasing the flexibility of the overall system. This is a significant development and is the main contribution of this research.

Section II developed the complex screen technique theoretically: First, the germane details of the complex screen approach were presented. Second, amplitude control using a single phase-only SLM was presented and discussed. Last, a generic phase-only SLM command, required to produce a single instance of a Schell-model source, was shown.

The technique was validated experimentally in Section III. Three Schell-model sources were generated in the laboratory. The first, a BGSM source (theoretically analyzed in past literature[22,36]), was chosen so that the theoretical predictions could be directly compared to experimental results. These results ultimately validated the proposed approach, as the agreement between theory, simulation, and experiment was quite good. The second and third Schell-model sources were sources that could not be generated using existing techniques. The NMSU AFIT and retina fingerprint Schell-model sources were generated with mixed results. The NMSU and AFIT logos were clearly reproduced and the agreement between the simulated and experimental results was excellent. While the fingerprint image was successfully reproduced, many key features in the generated retina scan images were lost. The retina fingerprint Schell-model source was at the limit of what could practically be synthesized using the validation setup. This was supported by the good agreement between the simulated and experimental retina fingerprint source results. Finally, the overall quality of the reproduced images and factors that must be considered when designing a system for a specific application were discussed.

The method introduced in this paper will be useful in any application where precise control over beam shape and coherence are important. Some of these applications include free-space optical communications, directed energy, material processing, and particle manipulation.

ACKNOWLEDGMENTS

The authors would like to thank Dr. Jack E. McCrae for many helpful discussions regarding this research.

This research was supported in part by an appointment to the Postgraduate Research Participation Program at the Air Force Institute of Technology administered by the Oak Ridge Institute for Science and Education through an interagency agreement between the U.S. Department of Energy and AFIT.

This work was supported by the Air Force Office of Scientific Research (AFOSR) Multidisciplinary Research Program of the University Research Initiative (MURI) Grant No. FA9550-12-1-0449.

The views expressed in this paper are those of the authors and do not reflect the official policy or position of the U.S. Air Force, the Department of Defense, or the U.S. Government.

[1]S. R. Seshadri, "Polarization properties of partially coherent Gaussian Schell-model electromagnetic beams," J. Appl. Phys. **87**, 4084–4093 (2000).
[2]S. R. Seshadri, "Spatial coherence of azimuthally symmetric Gaussian electromagnetic beams," J. Appl. Phys. **88**, 6973–6980 (2000).
[3]F. Wang, X. Liu, and Y. Cai, "Propagation of partially coherent beam in turbulent atmosphere: A review," Prog. Electromagn. Res. **150**, 123–143 (2015).
[4]S. Avramov-Zamurovic, C. Nelson, R. Malek-Madani, and O. Korotkova, "Polarization-induced reduction in scintillation of optical beams propagating in simulated turbulent atmospheric channels," Waves Random Complex Media **24**, 452–462 (2014).
[5]M. Salem, O. Korotkova, A. Dogariu, and E. Wolf, "Polarization changes in partially coherent electromagnetic beams propagating through turbulent atmosphere," Waves Random Media **14**, 513–523 (2004).
[6]Y. Cai, O. Korotkova, H. T. Eyyuboglu, and Y. Baykal, "Active laser radar systems with stochastic electromagnetic beams in turbulent atmosphere," Opt. Express **16**, 15834–15846 (2008).
[7]S. Sahin, Z. Tong, and O. Korotkova, "Sensing of semi-rough targets embedded in atmospheric turbulence by means of stochastic electromagnetic beams," Opt. Commun. **283**, 4512–4518 (2010).
[8]O. Korotkova and N. Farwell, "Effect of oceanic turbulence on polarization of stochastic beams," Opt. Commun. **284**, 1740–1746 (2011).
[9]G. Gbur, "Partially coherent beam propagation in atmospheric turbulence," J. Opt. Soc. Am. A **31**, 2038–2045 (2014).
[10]M. Yao, I. Toselli, and O. Korotkova, "Propagation of electromagnetic stochastic beams in anisotropic turbulence," Opt. Express **22**, 31608–31619 (2014).
[11]M. W. Hyde, S. Basu, M. F. Spencer, S. J. Cusumano, and S. T. Fiorino, "Physical optics solution for the scattering of a partially coherent wave from a statistically rough material surface," Opt. Express **21**, 6807–6825 (2013).
[12]M. W. Hyde, A. E. Bogle, and M. J. Havrilla, "Scattering of a partially coherent wave from a material circular cylinder," Opt. Express **21**, 32327–32339 (2013).
[13]M. W. Hyde IV, "Physical optics solution for the scattering of a partially coherent wave from a circular cylinder," Opt. Commun. **338**, 233–239 (2015).
[14]F. J. Torcal-Milla and L. M. Sanchez-Brea, "Gaussian-Schell-model beams propagating through rough gratings," J. Opt. Soc. Am. A **28**, 308–313 (2011).
[15]T. D. Visser, D. G. Fischer, and E. Wolf, "Scattering of light from quasi-homogeneous sources by quasi-homogeneous media," J. Opt. Soc. Am. A **23**, 1631–1638 (2006).
[16]T. van Dijk, D. G. Fischer, T. D. Visser, and E. Wolf, "Effects of spatial coherence on the angular distribution of radiant intensity generated by scattering on a sphere," Phys. Rev. Lett. **104**, 173902 (2010).

[17]D. G. Fischer, T. van Dijk, T. D. Visser, and E. Wolf, "Coherence effects in Mie scattering," J. Opt. Soc. Am. A **29**, 78–84 (2012).
[18]Z. Mei and O. Korotkova, "Random light scattering by collections of ellipsoids," Opt. Express **20**, 29296–29307 (2012).
[19]Y. Zhang and D. Zhao, "Scattering of multi-Gaussian Schell-model beams on a random medium," Opt. Express **21**, 24781–24792 (2013).
[20]J. Liu, L. Bi, P. Yang, and G. W. Kattawar, "Scattering of partially coherent electromagnetic beams by water droplets and ice crystals," J. Quant. Spectrosc. Radiat. Transfer **134**, 74–84 (2014).
[21]Y. Zhang and D. Zhao, "The coherence and polarization properties of electromagnetic rectangular Gaussian Schell-model sources scattered by a deterministic medium," J. Opt. **16**, 125709 (2014).
[22]Z. Mei and O. Korotkova, "Random sources generating ring-shaped beams," Opt. Lett. **38**, 91–93 (2013).
[23]O. Korotkova, "Random sources for rectangular far fields," Opt. Lett. **39**, 64–67 (2014).
[24]O. Korotkova and E. Shchepakina, "Random sources for optical frames," Opt. Express **22**, 10622–10633 (2014).
[25]Y. Zhang and Y. Cai, "Random source generating far field with elliptical flat-topped beam profile," J. Opt. **16**, 075704 (2014).
[26]D. Voelz, X. Xiao, and O. Korotkova, "Numerical modeling of Schell-model beams with arbitrary far-field patterns," Opt. Lett. **40**, 352–355 (2015).
[27]M. W. Hyde IV, S. Basu, X. Xiao, and D. G. Voelz, "Producing any desired far-field mean irradiance pattern using a partially coherent Schell-model source," J. Opt. **17**, 055607 (2015).
[28]Y. Chen, F. Wang, L. Liu, C. Zhao, Y. Cai, and O. Korotkova, "Generation and propagation of a partially coherent vector beam with special correlation functions," Phys. Rev. A **89**, 013801 (2014).
[29]Y. Chen, L. Liu, F. Wang, C. Zhao, and Y. Cai, "Elliptical Laguerre-Gaussian correlated Schell-model beam," Opt. Express **22**, 13975–13987 (2014).
[30]F. Wang, C. Liang, Y. Yuan, and Y. Cai, "Generalized multi-Gaussian correlated Schell-model beam: From theory to experiment," Opt. Express **22**, 23456–23464 (2014).
[31]M. Takeda, W. Wang, Z. Duan, and Y. Miyamoto, "Coherence holography," Opt. Express **13**, 9629–9635 (2005).
[32]L. Mandel and E. Wolf, *Optical Coherence and Quantum Optics* (Cambridge University, 1995).
[33]E. Wolf, *Introduction to the Theory of Coherence and Polarization of Light* (Cambridge University, 2007).
[34]*Vectorial Optical Fields: Fundamentals and Applications*, edited by Q. Zhan (World Scientific, 2014).
[35]G. Gbur and T. D. Visser, "The structure of partially coherent fields," in *Progress in Optics*, edited by E. Wolf (Elsevier, 2010), Vol. 55, Chap. 5, pp. 285–341.
[36]O. Korotkova, *Random Light Beams: Theory and Applications* (CRC, 2014).
[37]Y. Cai, Y. Chen, and F. Wang, "Generation and propagation of partially coherent beams with nonconventional correlation functions: A review," J. Opt. Soc. Am. A **31**, 2083–2096 (2014).
[38]Y. Cai, "Generation of various partially coherent beams and their propagation properties in turbulent atmosphere: A review," Proc. SPIE **7924**, 792402 (2011).
[39]S. Basu, M. W. Hyde, X. Xiao, D. G. Voelz, and O. Korotkova, "Computational approaches for generating electromagnetic Gaussian Schell-model sources," Opt. Express **22**, 31691–31707 (2014).
[40]C. Liang, F. Wang, X. Liu, Y. Cai, and O. Korotkova, "Experimental generation of cosine-Gaussian-correlated Schell-model beams with rectangular symmetry," Opt. Lett. **39**, 769–772 (2014).
[41]A. S. Ostrovsky, G. Martínez-Niconoff, V. Arrizón, P. Martínez-Vara, M. A. Olvera-Santamaría, and C. Rickenstorff-Parrao, "Modulation of coherence and polarization using liquid crystal spatial light modulators," Opt. Express **17**, 5257–5264 (2009).
[42]A. S. Ostrovsky, M. A. Olvera, C. Rickenstorff, G. Martínez-Niconoff, and V. Arrizón, "Generation of a secondary electromagnetic source with desired statistical properties," Opt. Commun. **283**, 4490–4493 (2010).
[43]A. S. Ostrovsky, G. Rodríguez-Zurita, C. Meneses-Fabián, M. A. Olvera-Santamaría, and C. Rickenstorff-Parrao, "Experimental generating the partially coherent and partially polarized electromagnetic source," Opt. Express **18**, 12864–12871 (2010).
[44]Y. Chen, F. Wang, C. Zhao, and Y. Cai, "Experimental demonstration of a Laguerre-Gaussian correlated Schell-model vortex beam," Opt. Express **22**, 5826–5838 (2014).
[45]F. Wang, X. Liu, Y. Yuan, and Y. Cai, "Experimental generation of partially coherent beams with different complex degrees of coherence," Opt. Lett. **38**, 1814–1816 (2013).
[46]F. Wang, Y. Cai, Y. Dong, and O. Korotkova, "Experimental generation of a radially polarized beam with controllable spatial coherence," Appl. Phys. Lett. **100**, 051108 (2012).
[47]F. Wang and Y. Cai, "Experimental generation of a partially coherent flat-topped beam," Opt. Lett. **33**, 1795–1797 (2008).
[48]T. Shirai and E. Wolf, "Coherence and polarization of electromagnetic beams modulated by random phase screens and their changes on propagation in free space," J. Opt. Soc. Am. A **21**, 1907–1916 (2004).
[49]T. Shirai, O. Korotkova, and E. Wolf, "A method of generating electromagnetic Gaussian Schell-model beams," J. Opt. A: Pure Appl. Opt. **7**, 232–237 (2005).
[50]M. Santarsiero, R. Borghi, and V. Ramírez-Sánchez, "Synthesis of electromagnetic Schell-model sources," J. Opt. Soc. Am. A **26**, 1437–1443 (2009).
[51]G. Piquero, F. Gori, P. Romanini, M. Santarsiero, R. Borghi, and A. Mondello, "Synthesis of partially polarized Gaussian Schell-model sources," Opt. Commun. **208**, 9–16 (2002).
[52]J. W. Goodman, *Statistical Optics* (Wiley, 1985).
[53]L. Zhu and J. Wang, "Arbitrary manipulation of spatial amplitude and phase using phase-only spatial light modulators," Sci. Rep. **4**, 7441 (2014).
[54]A. Siemion, M. Sypek, J. Suszek, M. Makowski, A. Siemion, A. Kolodziejczyk, and Z. Jaroszewicz, "Diffuserless holographic projection working on twin spatial light modulators," Opt. Lett. **37**, 5064–5066 (2012).
[55]A. Jesacher, C. Maurer, A. Schwaighofer, S. Bernet, and M. Ritsch-Marte, "Full phase and amplitude control of holographic optical tweezers with high efficiency," Opt. Express **16**, 4479–4486 (2008).
[56]A. Jesacher, C. Maurer, A. Schwaighofer, S. Bernet, and M. Ritsch-Marte, "Near-perfect hologram reconstruction with a spatial light modulator," Opt. Express **16**, 2597–2603 (2008).
[57]D. G. Voelz and X. Xiao, "Wave optics modeling and laboratory generation of 'exotic' partial coherent beams," in *Imaging and Applied Optics 2014* (Optical Society of America, 2014), p. PW2E.2.
[58]X. Xiao, O. Korotkova, and D. G. Voelz, "Laboratory implementation of partially coherent beams with super-Gaussian distribution," Proc. SPIE **9224**, 92240N (2014).
[59]J. P. Kirk and A. L. Jones, "Phase-only complex-valued spatial filter," J. Opt. Soc. Am. **61**, 1023–1028 (1971).
[60]J. Leach, M. R. Dennis, J. Courtial, and M. J. Padgett, "Vortex knots in light," New J. Phys. **7**, 55 (2005).
[61]E. Bolduc, N. Bent, E. Santamato, E. Karimi, and R. W. Boyd, "Exact solution to simultaneous intensity and phase encryption with a single phase-only hologram," Opt. Lett. **38**, 3546–3549 (2013).
[62]J. C. Vaughan, T. Hornung, T. Feurer, and K. A. Nelson, "Diffraction-based femtosecond pulse shaping with a two-dimensional spatial light modulator," Opt. Lett. **30**, 323–325 (2005).
[63]J. A. Davis, D. M. Cottrell, J. Campos, M. J. Yzuel, and I. Moreno, "Bessel function output from an optical correlator with a phase-only encoded inverse filter," Appl. Opt. **38**, 6709–6713 (1999).
[64]Z. Yu, H. Chen, Z. Chen, J. Hao, and J. Ding, "Simultaneous tailoring of complete polarization, amplitude and phase of vector beams," Opt. Commun. **345**, 135–140 (2015).
[65]Z. Chen, T. Zeng, B. Qian, and J. Ding, "Complete shaping of optical vector beams," Opt. Express **23**, 17701–17710 (2015).
[66]S. Ramo, J. Whinnery, and T. Van Duzer, *Fields and Waves in Communication Electronics*, 3rd ed. (Wiley, 1994).
[67]P. Ufimtsev, *Fundamentals of the Physical Theory of Diffraction* (IEEE, 2007).
[68]C. A. Balanis, *Antenna Theory: Analysis and Design*, 3rd ed. (Wiley, 2005).
[69]Boulder Nonlinear Systems, Inc., *Spatial Light Modulators—XY Series* (Retrieved November 16, 2013).
[70]Lumenera Corporation, *Lu120, Lu125 1.3 Megapixel USB 2.0 Camera* (Retrieved November 16, 2013).
[71]J. W. Goodman, *Introduction to Fourier Optics*, 3rd ed. (Roberts & Company, 2005).
[72]J. W. Goodman, *Speckle Phenomena in Optics: Theory and Applications* (Roberts & Company, 2007).